Research Paper

GEOSPHERE

GEOSPHERE

https://doi.org/10.1130/GES02961.1

13 figures; 1 set of supplemental files

CORRESPONDENCE: stefano.tavani@unifi.it

CITATION: Tavani, S., Mazzini, I., Agosta, F., Billi, A., Coli, M., Conti, J., Forti, L., Parente, M., Pizzati, M., Risaliti, G., Pieruccini, P., and Sardella, R., 2026, Structural geology and cave evolution at the gate of prehistory: The backbone of Grotta Romanelli, southern Italy: Geosphere, https://doi.org/10.1130/GES02961.1.

Science Editor: Andrea Hampel
Associate Editor: Michelangelo Martini

Received 28 February 2026
Revision received 20 April 2026
Accepted 11 May 2026

Published online 15 May 2026

Structural geology and cave evolution at the gate of prehistory: The backbone of Grotta Romanelli, southern Italy

S. Tavani[1,2], I. Mazzini[2], F. Agosta[3], A. Billi[2], M. Coli[1], J. Conti[4], L. Forti[5], M. Parente[6], M. Pizzati[7], G. Risaliti[1], P. Pieruccini[8], and R. Sardella[9]

[1]University of Florence, Department of Earth Sciences, Via La Pira 4, 50121, Florence, Italy
[2]Consiglio Nazionale delle Ricerche (CNR)–Institute of Environmental Geology and Geoengineering (IGAG), Piazzale Aldo Moro 5, 00185, Rome, Italy
[3]University of Basilicata, Department of Sciences, Via dell'Ateneo Lucano 10, 85100, Potenza, Italy
[4]University of Rome La Sapienza, Department of Antiquities, Piazzale Aldo Moro 5, 00185, Rome, Italy
[5]University of Milan, Department of Earth Sciences, Via Luigi Mangiagalli 34, 20133, Milan, Italy
[6]University of Naples Federico II, Department of Earth Sciences, Environment and Resources, Via Vicinale Cupa Cintia 21, 80126, Naples, Italy
[7]University of Parma, Department of Chemistry, Life Sciences and Environmental Sustainability, Parco Area delle Scienze 157/A, 43124, Parma, Italy
[8]University of Turin, Department of Earth Sciences, Via Valperga Caluso 35, 10125, Turin, Italy
[9]University of Rome La Sapienza, Department of Earth Sciences, Piazzale Aldo Moro 5, 00185, Rome, Italy

ABSTRACT

Grotta Romanelli (Romanelli Cave) stands as a key site of the European Paleolithic, preserving traces of human occupation since the middle Pleistocene. To date, little attention has been devoted to the carbonate bedrock that hosts the cavity, and to the role that tectonic structures played in its formation. To fill this gap, we conducted combined structural, petrophysical, and stratigraphic analyses, supported by the interpretation of a high-resolution 3-D virtual outcrop model of the cave and its surroundings. The results indicate that the cave was part of a system of Cretaceous extension-related structures affecting synkinematic carbonates. In particular, the cave opens within, and aligns with, an extensional fault–related anticline, which developed in the footwall of an embryonic extensional fault zone. The overall morphology of the cave and its progressive widening were strongly governed by exfoliation along preexisting discontinuities affecting synkinematic strata, namely, bedding planes and fault surfaces. Furthermore, the presence of porous, poorly lithified synkinematic Upper Cretaceous limestones, particularly at the thin entrance roof, raises critical stability concerns. The results of this integrated analysis, which provides the first geologically constrained 3-D model of the bedrock limestones of Grotta Romanelli, offer a robust basis for assessing the structural control, stability, and long-term evolution of the site. Results therefore enhance both scientific interpretation and management of limestone-hosted caves.

1. INTRODUCTION

Grotta Romanelli is located along the Adriatic coastline at the southern tip of the Apulian region of Italy (Fig. 1), and it is one of the first Italian caves where deposits with Paleolithic stone tools, fauna, and parietal art were described. Following its discovery in the late nineteenth century and subsequent major excavations (Stasi and Regalia, 1904; Blanc, 1920; Carandini and Bidditu, 1967), the Quaternary stratigraphic succession and chronological framework documented at Grotta Romanelli (Fornaca-Rinaldi, 1968) served as an important regional reference for both archaeological and paleontological research, encompassing a record that spans from the middle Pleistocene to the Upper Paleolithic (Cardini, 1963; Cassoli and Tagliacozzo, 1997; Sardella et al., 2019, and references therein), as well as for the reconstruction of past Mediterranean sea-level changes (Mastronuzzi et al., 2007; Benjamin et al., 2017; Antonioli et al., 2018). Recent excavations and geoarchaeological work at Grotta Romanelli have revised the cave's sedimentary infill and chronology (Pieruccini et al., 2022), revealing multiple stratigraphic units formed from the middle Pleistocene to the early–middle Holocene (Tema et al., 2025) and, crucially, clear evidence of human activity throughout this interval. The cave infill is characterized by multiple Quaternary paraconformities, consisting of nondepositional surfaces documented throughout the sedimentary succession, and abrupt episodes of sediment accumulation. The walls of the cave also preserve evidence of parietal art, making Grotta Romanelli one of the most remarkable expressions of the late Upper Paleolithic symbolic behavior in the Mediterranean (Sigari et al., 2024). Outside the cave, Quaternary slope deposits are present, partly damming the cave entrance. These deposits consist of coarse- to very coarse-grained, cemented debris-slope deposits and shoreface gravels and pebbles (Pieruccini et al., 2022).

While Quaternary deposits exposed at Grotta Romanelli, as well as their archaeological and paleoenvironmental significance, have long been studied, the geological context of the cavity, namely, the nature and structure of the Cretaceous carbonate bedrock in which it occurs, has received comparatively little attention. Yet, understanding this framework is essential for reconstructing the cave's morphogenesis (e.g., White, 1988; Ford and Williams, 2007; Silva et al., 2017; Antonellini et al., 2019; De Waele and Gutiérrez, 2022) and,

Stefano Tavani https://orcid.org/0000-0003-3033-5314

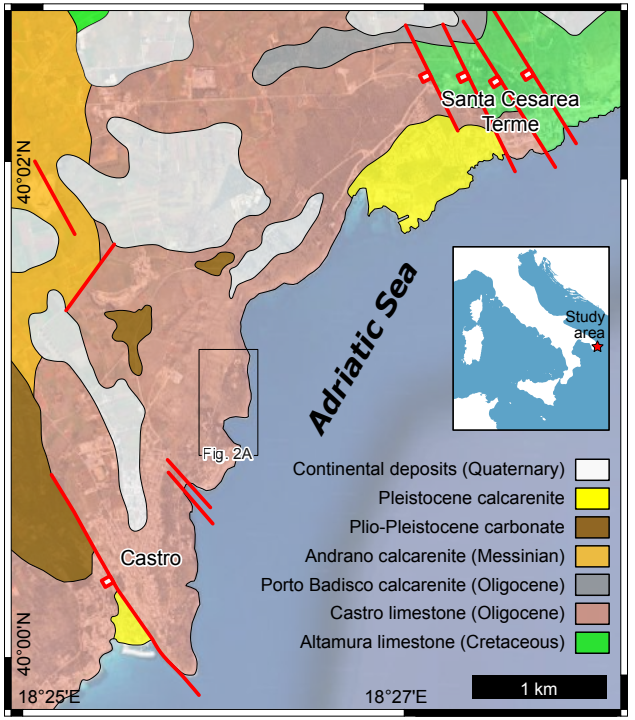

Figure 1. Geologic map of the area between Castro and Santa Cesarea Terme (after Bosellini et al., 1999; Santaloia et al., 2016). Inset shows the location of the study area within the Italian peninsula.

ultimately, assessing its stability (e.g., Goodman, 1989; Palmer, 2007; Xiao et al., 2025). Indeed, it is well established that cave development in carbonate settings is often controlled by tectonic structures like folds and fault systems (e.g., Palmer, 1989; Goldscheider and Neukum, 2010; Ennes-Silva et al., 2016; Bagni et al., 2020), which promote mechanical (fracturing) and chemical (dissolution) alteration of limestones (Palmer, 2007) and favor the alignment of caves along these structural zones of enhanced permeability (Abolins et al., 2025). However, the integration of surface (outside) and subsurface (inside) geological surveys remains a significant challenge (e.g., Boersma et al., 2019; Pennos et al., 2019; Comina et al., 2024), often resulting in an incomplete understanding of the links between tectonic architecture and speleogenesis, which in the case of Grotta Romanelli is not yet understood.

Motivated by the aforementioned aims and challenges, we carried out a combined on-site and digital structural, stratigraphic, and petrophysical study of the Cretaceous bedrock exposed in the area of the Grotta Romanelli. Our study tested the hypothesis that the cave's location, internal geometry, and morphological evolution were directly controlled by Cretaceous structures, as well as lithological and petrophysical characteristics of the Cretaceous succession. In detail, we investigated how an embryonic, synsedimentary extensional fault and the resulting lateral juxtaposition of lithofacies with contrasting mechanical properties provided the primary framework for subsequent speleogenesis and the cave's present-day stability. Field surveying in the bay hosting the cave was complemented by the structural interpretation of a virtual outcrop model (VOM) covering both the coastal cliff and the cave, which allowed us to accurately map subtle structural features, providing the geometric foundation for building cross sections of the cave. This integrated approach aimed to define the tectono-sedimentary setting of the area, with particular emphasis on the recognition of bedding surfaces, fracture zones, deformation bands, and major fault zones, as well as on the assessment of the potential control(s) by the aforementioned depositional and structural elements on speleogenesis. In this regard, to provide a quantitative basis for evaluating the influence of the structural framework on cave development, we integrated petrographic and petrophysical characterizations (the relative rock strength and air permeability) of the Mesozoic bedrock. These data were essential to document how deformation and primary depositional facies created the mechanical heterogeneities that produced selective erosion.

In the following sections, we describe the geological setting of Romanelli Bay and Grotta Romanelli, present the results of our integrated field and digital survey, and analyze the structural and petrophysical properties of the Cretaceous bedrock. These datasets are then combined into a workflow that moves from structural and stratigraphic characterization, through petrophysical quantification, to mechanical stability assessment. The latter includes a finite element method (FEM) numerical simulation used to validate the influence of the mapped structural discontinuities on the cave's stress field and current morphology. This approach provides a comprehensive geological framework for Grotta Romanelli, highlights the critical influence of preexisting tectonic structures on its speleogenesis, and offers a novel methodology for geohazard evaluation in comparable karstic environments.

2. GEOLOGICAL SETTING

Grotta Romanelli is located at the southern tip of the Salento Peninsula (Apulia region, Fig. 1) in the foreland of the Apenninic fold-and-thrust belt. There, the marine cliffs expose subhorizontal to gently dipping Mesozoic–Cenozoic carbonates that represent the southeastern margin of the Apulian carbonate platform (Bosellini et al., 1999). The Apulian carbonate platform is one of the carbonate platforms that developed at the southern margin of the Tethyan Ocean (Bernoulli, 2001). Its stratigraphic succession consists almost entirely of Upper Triassic–Upper Cretaceous shallow-water carbonates, >6 km thick (Ricchetti et al., 1988), unconformably overlain by thin sequences of Cenozoic carbonates (Bosellini and Russo, 1992; Bosellini et al., 1999; Pomar et al., 2014). Grotta Romanelli, the entrance of which lies 7 m above the present-day

sea level, faces Romanelli Bay, in between the villages of Castro and Santa Cesarea Terme (Fig. 1). This part of the coast exposes the Upper Oligocene coral-rich Castro Limestone Formation, with only limited outcrops of the Upper Cretaceous Ciolo Limestone and of the Middle Eocene Torre Tiggiano Limestone Formation, and it is affected by NW-SE–striking, high-angle extensional faults (e.g., Bosellini et al., 1999; Santaloia et al., 2016). Focusing on the Romanelli Bay, both Upper Cretaceous and Upper Oligocene carbonates are exposed (Fig. 2). The flanks of the bay are characterized by vertical cliffs exposing the clinostratified calcarenites and calcirudites of the Upper Oligocene Castro Limestone Formation, which unconformably overlie an ~50-m-thick succession of Maastrichtian limestones exposed in the central part of the bay. These limestones have no known correlatives in the surrounding region and are here informally referred to as the Romanelli limestones. Within this unit, we distinguish three lithofacies, which essentially differ only in their degree of cementation (lithofacies A and C are cemented, while lithofacies B is poorly cemented). In the inner part of the bay, characterized by a gentler slope, the Cretaceous Romanelli limestones are partially covered by Quaternary deposits. These Cretaceous limestones are folded into a SE-plunging anticline (Figs. 2B and 3A), crosscut southeastward by a NE-SW–striking, high-angle extensional fault sealed by the Castro Limestone Formation. The Romanelli limestones exposed in the hanging wall of this fault, as well as those occurring at the lowermost part of the footwall, are well lithified and correspond to lithofacies C and A, respectively. In contrast, the upper portion of the footwall succession consists of poorly lithified and porous limestones (Figs. 3 and 4), pervasively cut by tabular deformation bands. This portion belongs to lithofacies B of the Romanelli limestones, which also occurs in a patch in the hanging wall of the

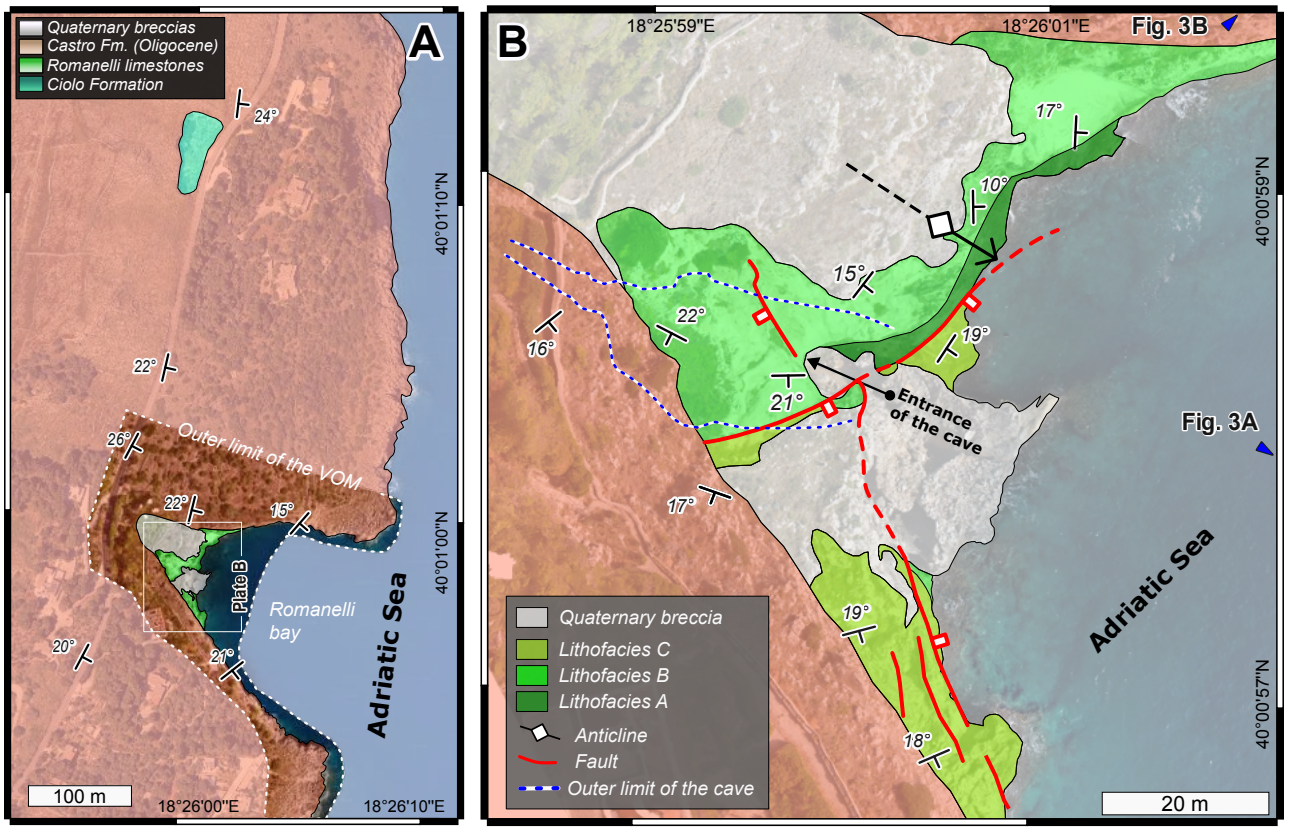

Figure 2. (A) Geologic map of Romanelli Bay and its surroundings. (B) Original detailed geologic map of the portion of the bay hosting Grotta Romanelli, showing the subsurface extent of the cave, major faults, bedding attitudes, fold axes, the Cretaceous anticline, and the main normal fault. VOM—virtual outcrop model.

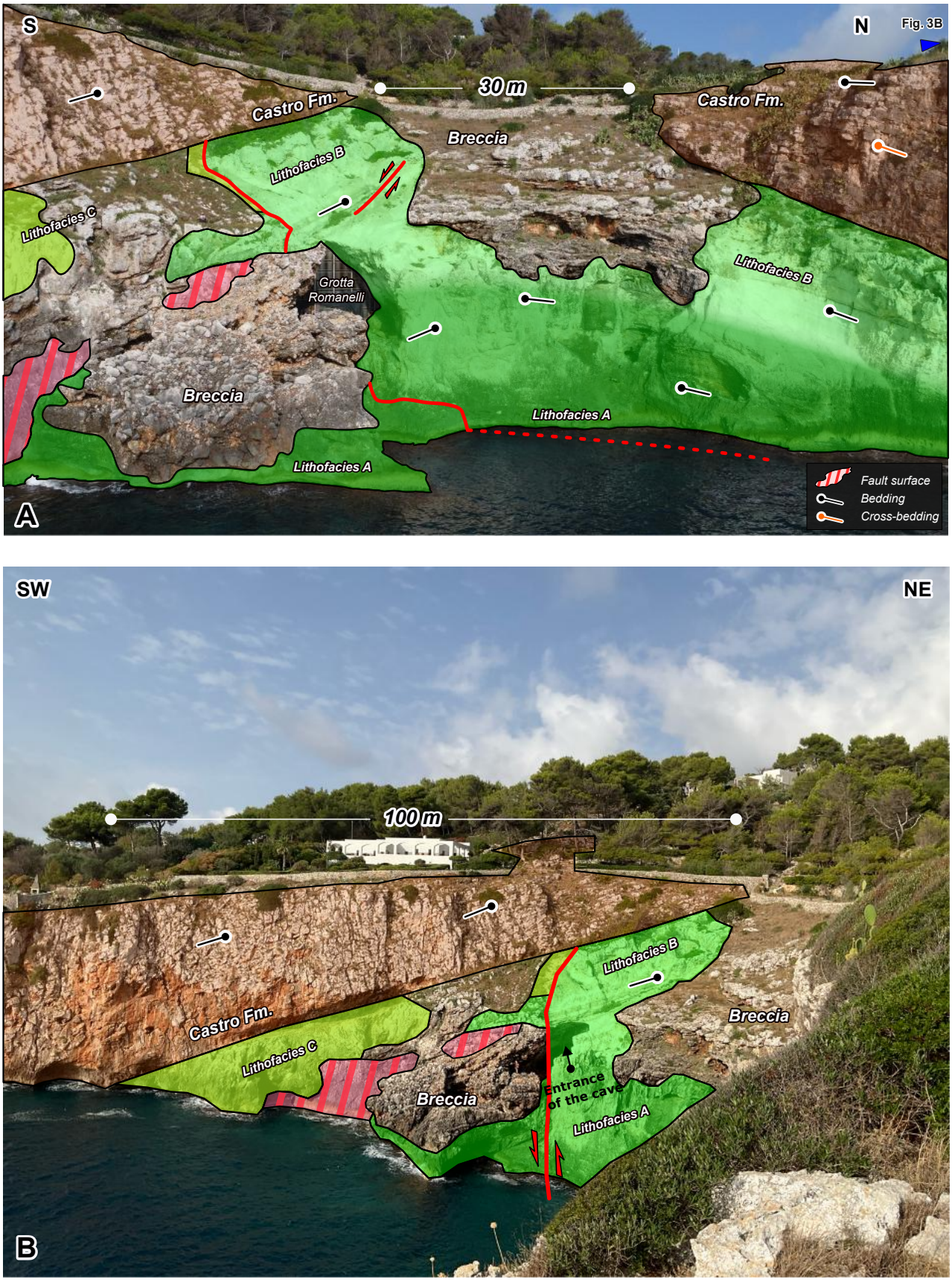

Figure 3. (A) Frontal view of the Cretaceous anticline at Romanelli Bay. (B) View perpendicular to image in A, showing the NE-SW–striking fault and the Castro Limestone Formation sealing the fault plane.

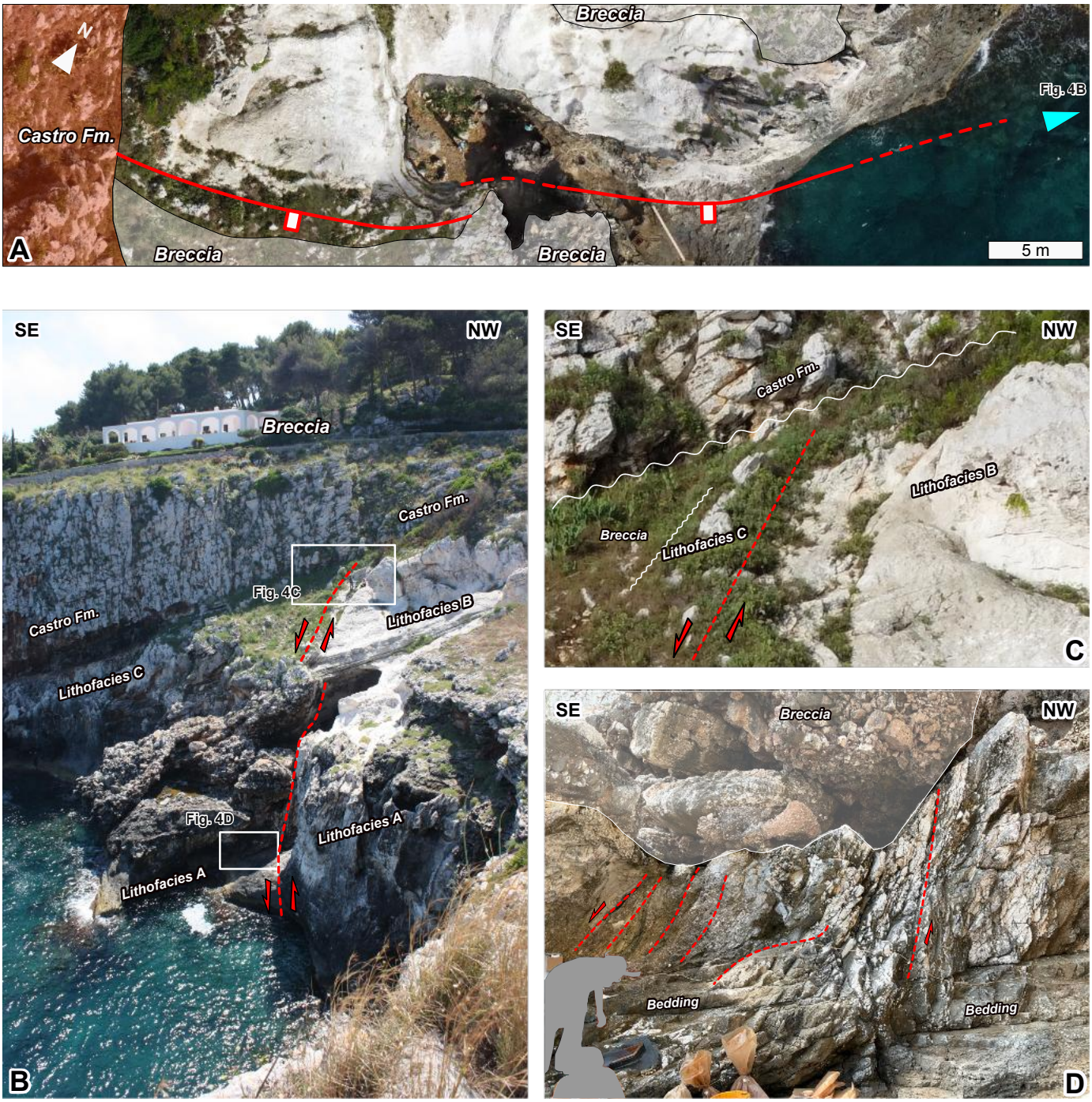

Figure 4. Detailed view of the NE-SW–striking fault. (A) Orthophoto showing the mapped fault trace. (B) Photograph parallel to the fault strike. (C) Upper segment of the fault, juxtaposing lithofacies B in the footwall with lithofacies C in the hanging wall; the Castro Limestone Formation caps and seals the fault. (D) Fault exposure at sea level, showing an array of extensional duplexes.

NE-SW–striking fault (Fig. 4B). The occurrence of this patch, together with the observation that both the hanging wall and footwall expose lithofacies A at the lower tip of the NE-SW–striking fault (Fig. 4B), constrains the displacement along the fault to ~20 m. At the center of the bay lies the entrance to Grotta Romanelli, which extends for nearly 40 m into lithofacies A and B, following a WNW-ESE trend.

3. MATERIALS AND METHODS

3.1 Virtual Outcrop Model

The VOM integrated image datasets were acquired with an uncrewed aerial vehicle (UAV; DJI Mini 4K), a digital single-lens reflex camera (dSLR; Canon EOS R100), and a smartphone with light detection and ranging (LiDAR) scanner (iPhone 13 Pro). The UAV dataset provided broad aerial coverage of the bay and cave entrance, the dSLR dataset targeted the cave interior, and the smartphone LiDAR-photogrammetry dataset was used to capture overhanging surfaces and narrow passageways. Datasets were processed using standard structure-from-motion and multiview stereo (SfM-MVS) workflows in Agisoft Metashape (e.g., Verhoeven, 2011; Tavani et al., 2019), merged using manually placed common markers, and georeferenced by alignment with a 50 cm/pixel (px) orthophoto and a 1:5000 topographic map. Final refinement was achieved using 45 sea-level markers to finely correct model orientation (tilt) and control points measured inside the cave to calibrate vertical positioning. The final VOM was cropped to remove nongeological elements (i.e., vegetation, buildings, sea), including the gate at the entrance of the cave, and used for four main purposes: (1) generation of a high-resolution orthophoto for geological mapping, (2) digital extraction of bedding and fault attitudes in the bay, (3) detailed structural and stratigraphic survey of the cave interior, and (4) extraction of cross sections along the cave axis to analyze the relation between the cave morphology and the tectono-stratigraphic framework. Full technical acquisition and processing details are reported in Supplemental Text S1.[1]

3.2 Geological Mapping

The geological survey was conducted using a 2 cm/px zenithal orthophoto derived from the VOM as a base map and resulted in the production of the original geological map in Figure 2B. Bedding plane data were collected in the field using the StraboField app (Walker et al., 2019) on an iPad Mini and an iPhone 13 Pro. Both devices have an intrinsic positioning error of ~5 m (Tavani et al., 2022). However, by repositioning these measurements on the georeferenced orthophoto, characterized by a verified horizontal accuracy of ~1 m, we were able to constrain the overall positional uncertainty of the structural data to within 1–2 m.

In addition to field measurements, geological mapping was also carried out by integrating observations from the VOM for inaccessible areas. The combined field and digital mapping aimed to reconstruct the geometry of the fold, the unconformity between the Cenozoic and Cretaceous packages, the limits between the Cretaceous subunits, and the attitudes of the main faults exposed in the Romanelli Bay area. Particular attention was given to the spatial relationships, intersection geometry, and vertical persistence of the faults.

3.3 Microfacies Analysis

Efforts were made to carefully map the boundaries between the three lithofacies within the Cretaceous Romanelli limestones. In particular, lithostratigraphic and biostratigraphic observations at the outcrop scale on the Romanelli limestones exposed in Romanelli Bay were complemented by optical microscope analysis of thin sections from 10 samples.

3.4 In Situ Petrophysical Analyses

The three lithofacies of the Romanelli limestones were analyzed by means of in situ Schmidt hammer tests and air permeability measurements. The relative rock strength was calculated after Schmidt hammer tests. At each site, 30 measurements were collected, and the average rock strength value was calculated after discarding the lowest 15 values. The in situ permeability values were determined by performing three measurements at each site using a New England Research Tiny Perm 3 portable air mini-permeameter. In the poorly lithified limestones of lithofacies B, direct measurements within deformation bands were also performed.

3.5 FEM Modeling

To preliminarily evaluate the mechanical stability of the Grotta Romanelli vault, we employed a FEM approach. Profiles of the cave derived from the VOM were used as the geometrical basis for building the numerical mesh. The model was partitioned into different rock masses (e.g., lithofacies A and B of the Romanelli limestones and Castro Limestone Formation) based on the geological mapping. We assigned mechanical properties (i.e., Young's modulus, Poisson's ratio, and cohesion) to each rock mass based on reference values for the lithotype. Density was measured on representative

[1]Supplemental Material. Technical details on the 3-D virtual outcrop model construction, including image acquisition and processing workflows, and rock mass mechanical properties and parameters adopted for the finite element method stability analysis. Please visit https://doi.org/10.1130/GEOS.S.32248326 to access the supplemental material, and contact editing@geosociety.org with any questions.

samples. The model was constrained by applying gravitational loads and boundary conditions to simulate the in situ stress state. The FEM analysis was performed using PHASE² v. 6.0 software (Rocscience, Inc.) to calculate the stress and strain distribution within the rock mass. The results of this analysis were then used to identify potential zones of instability, such as areas with high tensile stress, providing a preliminary assessment of the rockfall hazard at the cave entrance and along the vault. Additional details are provided in Supplemental Text S2.

4. RESULTS

4.1 Upper Cretaceous Limestones of Romanelli Bay

Here, we present the results acquired for the Romanelli limestones derived from integrated field mapping, microfacies analysis, and biostratigraphic data, part of which were introduced in the Geological Setting section for a narrative clarity.

The Romanelli limestones are fine grained, contain rudist fragments, and are composed of three different lithofacies. Two of these lithofacies, labeled as A and C, include well-lithified, whitish micritic limestones, occurring both in the hanging wall of the NE-SW–striking, high-angle extensional fault, and in the lowermost part of the fault footwall (Figs. 2 and 3). The third lithofacies, labeled as B, consists of poorly lithified, porous limestones occurring in the upper portion of the footwall block of the major NE-SW–striking fault, as patches in the hanging wall of the same fault, and along the southernmost portion of the Grotta Romanelli vault. These limestones are remarkably different from the coarse-grained, rudist-rich lithofacies of the Ciolo Limestone (Parente, 1994; Bosellini et al., 1999; Schlüter et al., 2008), which crops out in an abandoned quarry ~300 m to the north (Fig. 5A).

The microfacies of lithofacies A and C consist mainly of wackestones with fine-grained (mainly silt-sized) fragments of echinoderms, rare planktic

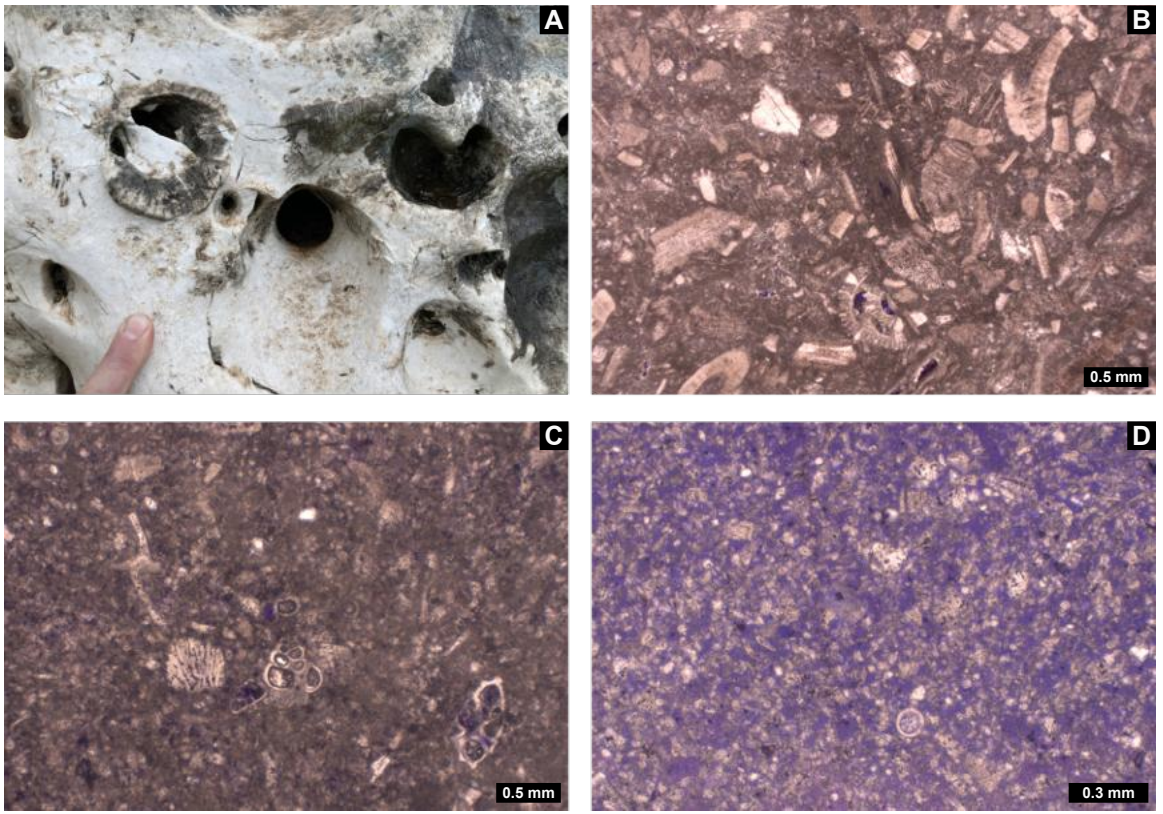

Figure 5. (A) Field view of the coarse-grained rudist-rich lithofacies of the Ciolo Limestone, exposed in an abandoned quarry ~300 m north of Grotta Romanelli. (B, C) Thin sections of the well-lithified whitish micritic limestones of lithofacies A and C, consisting mainly of wackestones with fine-grained echinoderm fragments, rare planktic foraminifers (globotruncanids and heterohelicids), and rudist fragments. (D) Thin section of the poorly lithified, very porous limestone of lithofacies B, showing a fine-grained grainstone composed mainly of silt- to fine sand–sized echinoderm fragments and rare calcispheres. The thin section has been impregnated with blue resin to emphasize porosity.

foraminifers (globotruncanids and heterohelicids), and sand-sized rudist fragments (Figs. 5B and 5C). More rarely, there are coarser-grained packstones with rudist fragments, echinoderm debris, and benthic foraminifers (fragments of *Omphalocyclus*, spines of *Siderolites*, and embryos and fragments of *Orbitoides*). The microfacies of lithofacies B consist of very porous fine-grained grainstone mainly made of silt- to fine sand–sized fragments of echinoderms, with rare calcispheres (Fig. 5D). In agreement with their fossil content, all carbonate lithofacies are attributed to the Maastrichtian; i.e., the Romanelli limestones are roughly coeval with the Ciolo Limestone but never documented stratigraphically below it. On the other hand, the top of the Ciolo Limestone is everywhere represented by an erosional surface, suggesting that the Romanelli limestones exposed at Romanelli Bay are the remnants of an unevenly distributed lithostratigraphic unit that once overlaid the Ciolo Limestone and is now largely eroded.

4.2 Bedding, Orthorectified Model, and Cross Section of Romanelli Bay

The bedding plane data for the Romanelli limestones and Castro Limestone Formation are reported in Figure 6. Data include the results of both manually and digitally collected measurements, as well as those after digital measurement of the unconformity surface in between the two formations. Manually collected bedding plane azimuth ranges from N-S to WNW-ESE (Fig. 6A), whereas the digitally collected bedding planes within the Cretaceous Romanelli limestones form two distinct clusters, defining E-dipping and S-dipping surfaces (Fig. 6B), respectively corresponding to the NE and SW limbs of an anticline. The unconformity surface between Mesozoic and Cenozoic carbonates is nonplanar; it dips toward SW along the SW limb of the anticline and NE along its NE limb (Fig. 6B). The digitally measured bedding surfaces within the Castro Limestone Formation along the northern cliff of the bay show a bimodal distribution, corresponding to gently SE-dipping planes and secondary NE-dipping clinoforms (Fig. 6C). Along the southern cliff, digitally measured bedding surfaces dip consistently SE (Fig. 6D). Figure 6E summarizes the results of digitally measured bedding surfaces (and clinoforms) and of the unconformity surface exposed on both limbs of the anticline. The poles are well clustered along a great circle, π, also reported in Figure 6D. The ~N120° (note: all strike and trend values in this study are reported using the N0°–360° azimuthal notation) subhorizontal β axis of the aforementioned π great circle was used as a viewing direction to generate the orthorectified image of the VOM (Fig. 6F), to minimize the obliquity of all the studied geological features (e.g., Tavani et al., 2016; Cawood et al., 2022). The interpreted orthorectified image (Fig. 6G) shows both bedding planes and clinoforms. To further clarify the geometric relationship between the Castro Formation and the underlying Romanelli limestones, we applied a restoration of the orthorectified cross section using the flexural-slip unfolding algorithm in 3DMove (Petex Ltd.), with Figure 6H showing the restored state obtained by unfolding the basal portion of the Castro Formation to the horizontal plane.

4.3 Mesoscale and Microscale Structural Analysis

Faults crosscutting the Romanelli limestones form three sets (Fig. 7) striking ~N150° (set F1), ~N30° (set F2), and ~N60° (set F3), respectively. Both sets F1 and F3 are approximately orthogonal to each other and occur in both manually and digitally collected datasets. In contrast, the F2 set was identified only in the manually collected fault dataset. The subvertical deformation bands, which pervasively affect lithofacies B (Figs. 8A and 8B), show a wide azimuthal dispersion in their strike directions, ranging between N135° and N195° (cf. Fig. 7). The mean strike direction of the deformation bands is broadly parallel to the F1 fault set. Microstructural analysis revealed pronounced grain-size reduction and cataclasis within deformation bands (Fig. 8C), which are hence classified as shear bands. Within lithofacies A and C, fractures do not take up any appreciable component of slip. Fractures form two main subvertical sets (cf. Fig. 7), respectively striking ~N45° and roughly N-S. In contrast, both high-angle faults and fractures affecting the Castro Limestone Formation consistently strike around N30°.

4.4 Petrophysical Analysis

Figure 9 includes the results of relative rock strength and permeability measurements. Data were acquired within an area exposing an ~50-m-thick stratigraphic section (Figs. 9A and 9B) composed of Cretaceous well-lithified limestones of lithofacies A at the bottom and lithofacies B at the top. The stratigraphically highest measurement site (site 5 in Fig. 9) was on lithofacies C lying at the hanging wall of a normal fault, juxtaposing lithofacies C against lithofacies B in the fault footwall. Lithofacies A and C showed a rock mass quality (Q) value (e.g., Katz et al., 2000) ranging from 50 to 70, whereas lithofacies B showed a median Q value of ~30 (Fig. 9C). The air permeability of lithofacies C was ~5 mD, whereas that of lithofacies B ranged from 40 mD to 300 mD (Fig. 9D). Notably, the permeability of deformation bands within lithofacies B (cf. Fig. 8B) dropped to ~5 mD (Fig. 9D). The different behavior of the two facies was also recorded by the different bulk densities of samples, ~1700 kg/m^3 for the porous and poorly cemented lithofacies B and ~2400 kg/m^3 for the lithified lithofacies A and C.

4.5 Structural Setting of Grotta Romanelli

Results of the combined digital and field surveys around Grotta Romanelli are reported in Figure 10. The cave floor exposes well-lithified lithofacies A, with beds dipping 8° toward the east. Outside of the cave, immediately above

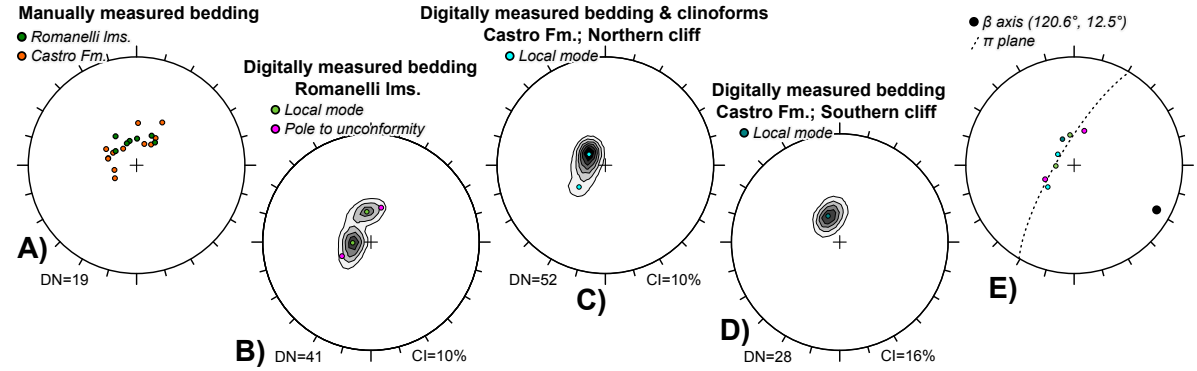

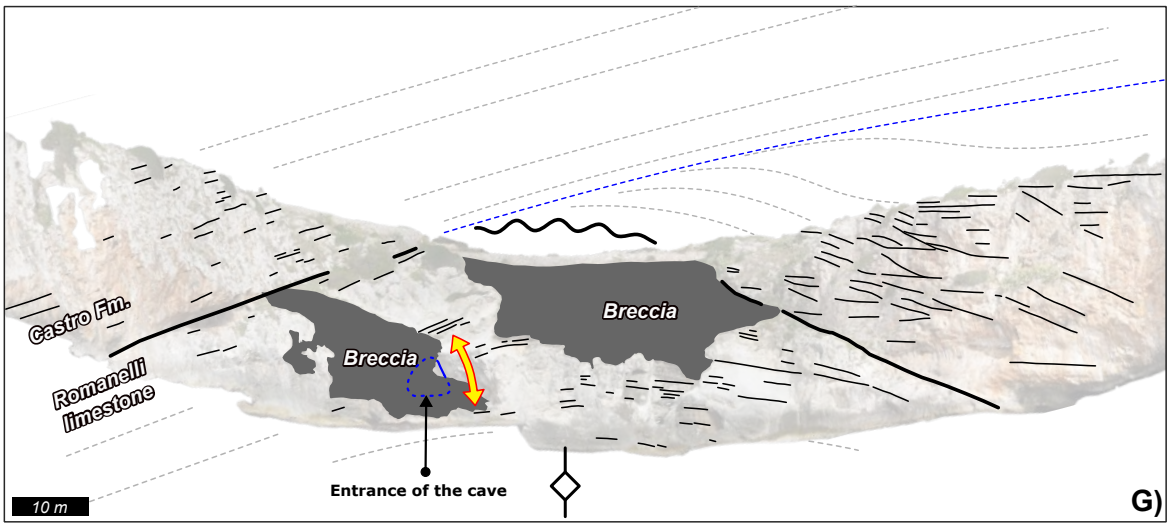

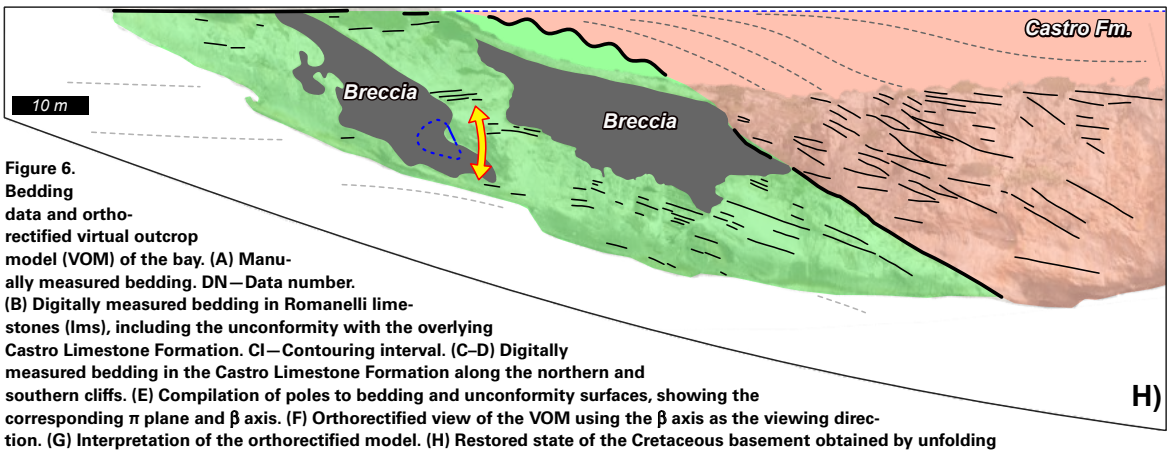

Figure 6. Bedding data and orthorectified virtual outcrop model (VOM) of the bay. (A) Manually measured bedding. DN—Data number. (B) Digitally measured bedding in Romanelli limestones (lms), including the unconformity with the overlying Castro Limestone Formation. CI—Contouring interval. (C–D) Digitally measured bedding in the Castro Limestone Formation along the northern and southern cliffs. (E) Compilation of poles to bedding and unconformity surfaces, showing the corresponding π plane and β axis. (F) Orthorectified view of the VOM using the β axis as the viewing direction. (G) Interpretation of the orthorectified model. (H) Restored state of the Cretaceous basement obtained by unfolding the basal portion of the Castro Formation (blue dashed line). This unfolding highlights the preexisting synsedimentary geometry of the Cretaceous anticline and its relationship with the prograding Oligocene infill.

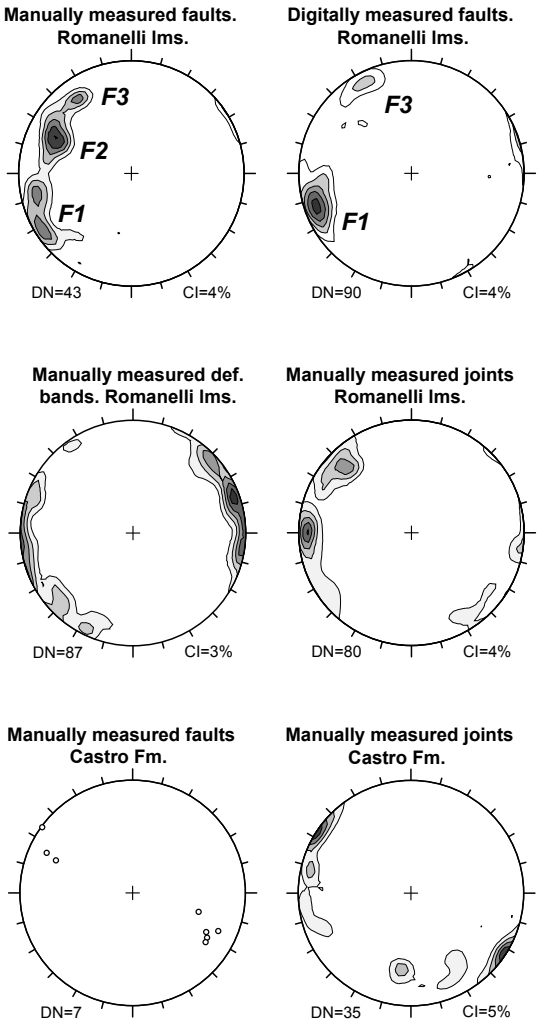

Figure 7. Comparison between manually and digitally measured structural data regarding faults, deformation bands, and joints. lms—limestones; DN—Data number; CI—Contouring interval.

its vault, lithofacies B beds dip ~25° toward the south (Fig. 10A). Within the cave, the vault occurs within the uppermost portion of well-lithified lithofacies A, as demonstrated by two different roof-spall deposits consisting of very coarse-grained, lithified limestone gravels, pebbles, and boulders (ISU 2 and ISU 4) interbedded within the Quaternary cave-filling succession (Fig. 11A; Pieruccini et al., 2022). Gently dipping discontinuities, of uncertain geological significance, are exposed on the vault and flanks of the cave (Fig. 11B). These discontinuities are weathered and covered by mold, and, above all, many of them were used for parietal art (Fig. 11C). The discontinuities undulate, so that, ultimately, their nature is not easily detectable in the field. We digitally measured these discontinuities on a VOM of the cave; results are consistent with the presence of three distinct sets (Fig. 10B): (1) Set D1 consists of gently NNE-dipping discontinuities, mainly occurring along the northern side of the cave; (2) set D2 is defined by a broad cluster, including planes parallel to bedding at the cave floor and vault; and (3) set D3 includes a limited number of planes dipping SSW. The β axis computed from the aforementioned three sets and the bedding planes above and at the base of the cave trends ~N103°E and plunges 8°. This β axis was then used to construct an orthorectified image of the cave and its entrance, with the β axis serving as the viewing direction. In doing so, the Quaternary breccia partly occluding the view of the cave entrance was digitally removed (Figs. 10D–10F). The interpretation of the obtained image shows that subhorizontal to gently NNE- and SSW-dipping discontinuities along the cave vault are nearly parallel to the overlying and underlying bedding, and together they form an open anticline. In contrast, the ~30° NNE-dipping discontinuities of set D1 exposed along the northern side of the cave are oblique to bedding; they collectively define a 2–3-m-thick tabular zone mimicking a normal fault zone putting in contact lithofacies A and B.

We also used the N103° trend of the β axis (Fig. 10C) to generate seven vertical slices (striking N13°) of the cave (Fig. 12). These slices show that the cave geometry resembles that of the anticline, which is only detectable in lithofacies A. Indeed, the beds of lithofacies A and B are parallel to each other on the southern limb of the anticline, whereas on the northern limb, they are discordant, with the beds of lithofacies B wedging above a zone affected by the faults.

4.6 FEM Modeling

FEM analyses were performed on sections 1 and 2 of Figure 12. The first section represents the main slopes immediately in front of the cave entrance, whereas the second depicts the cave profile just beyond the entrance (Fig. 13). The parameters adopted for the modeling are reported in Supplemental Text S2.

The obtained results, illustrated in Figure 13 as total estimated displacement (both as vector fields and as contour maps of displacement localization), indicate an overall good stability of both the slopes and the cave. In section 2, the calculated strength reduction factor (SRF) is 2.96, while in section 1, the software did not converge to a failure solution even after 200 iterations, suggesting that the corresponding SRF is significantly higher than that of section 2. Nevertheless, in section 2, displacement localization occurs within the "bridge" above the roof of the cave entrance. This implies that, should the mechanical

Figure 8. (A) Plan view of the limestones of lithofacies B showing multiple sets of mutually crosscutting deformation bands. (B) In situ measurement of the air permeability along a deformation band. (C) Photomosaic showing microstructural details of deformation bands with cataclastic reduction of particle size and porosity diminishing within the bands compared to the porous host rock.

properties of the rock mass decrease, this area would represent the most likely locus of incipient instability.

It should be emphasized that the models were constructed using reference mechanical parameters. Therefore, the interpretations discussed in section 4.4 provide a preliminary, first-order assessment of the overall stability of the rock mass. Further site-specific data on the lithological and mechanical properties of the involved rock masses are required to refine the simulation and to better constrain the mechanical behavior of the cave vault under stress.

5. DISCUSSION

5.1 Structural Setting and Timing of Deformation

Romanelli Bay is characterized by a prominent, ~100-m-wide open anticline involving the Maastrichtian Romanelli limestones. The fold plunges gently toward the southeast, it is sealed by the Oligocene calcarenites of the Castro Limestone Formation, and it is assessed as Maastrichtian in age due to the following evidence: (1) wedging of the Romanelli limestones (Fig. 6G), (2) synsedimentary faulting (Figs. 11 and 12), (3) soft-sediment shear banding (Fig. 8), and (4) sealing of the major bounding fault with the overlying Castro Limestone Formation (Figs. 3 and 4). Accordingly, the open anticline is interpreted as an extensional fault–related fold (e.g., Coleman et al., 2019) associated with an underlying NE-dipping bounding fault. The lack of contractional features at both map scale and mesoscale/microscale within the study area supports this interpretation. In fact, although contractional structural elements can form within extensional settings (e.g., Antonellini et al., 2008), their occurrence is not common (Agosta et al., 2010).

The Cretaceous succession is unconformably overlain by the Upper Oligocene Castro Limestone Formation, which prograded toward the NE, infilling the extensional, fault-related accommodation space produced during Cretaceous deformation (Fig. 6H). The occurrence of minor post-Oligocene tilting and fold amplification (<5°) is shown by the nonparallel bedding attitudes documented for the Oligocene Castro Formation on opposing cliffs of the bay (Figs. 6G and 6H). The latter episode could have been the result of regional-scale post-Oligocene forebulging of the Apulian carbonates (e.g., Argnani et al., 1993).

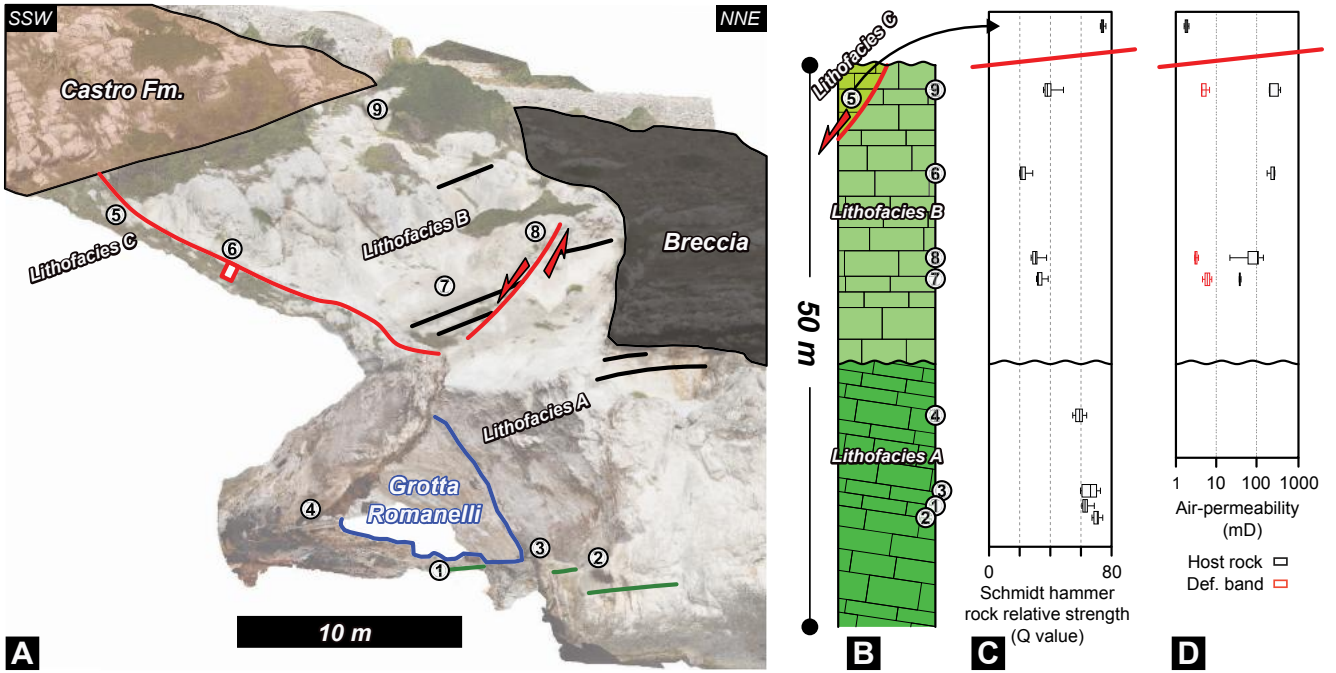

Figure 9. Summary of petrophysical and mechanical measurements in the Romanelli limestones. (A) Interpreted view of the sampling area. (B) Stratigraphic position of the samples. (C) Relative rock strength measurements. (D) Air permeability measurements.

Forebulging, which is expected to produce normal faulting and widespread jointing both parallel and perpendicular to the forebulge axis (e.g., Zhao and Jacobi, 1997; Lash and Engelder, 2007), in the study area resulted in NW-SE– and NE-SW–striking extensional structures (Billi and Salvini, 2003; Agosta et al., 2023). Accordingly, the joints and small normal faults crosscutting the Castro Limestone Formation (Fig. 7), as well as the NW-SE–striking normal faults involving Pleistocene deposits in the surroundings of Romanelli Bay (Fig. 1; Santaloia et al., 2016), are interpreted as having formed during this peripheral bulging stage of deformation.

In contrast, placing the Cretaceous deformation into a broader tectonic framework remains more challenging. Extensional structures of Aptian/Albian to Late Cretaceous age are widespread and well documented across Adria (e.g., Graziano, 2000; Bertok et al., 2012; Santantonio et al., 2013; Cipriani, 2016; Basilone and Sulli, 2018; Agosta et al., 2021). While those of late Early Cretaceous age have been convincingly linked to a specific tectonic phase (e.g., Tavani et al., 2023), the Late Cretaceous extensional structures of the Apulian region (e.g., Festa, 2003), including those described at Grotta Romanelli, are less well constrained. The Maastrichtian deformation documented in this work may therefore belong to a broader, but still poorly understood, episode of regional extension for which a definitive tectonic origin has yet to be demonstrated.

5.2 Mechanical Properties and Deformation Mechanisms

The Romanelli limestones display a pronounced mechanical contrast between the well-lithified lithofacies A and C and the porous, weakly cemented lithofacies B. In situ measurements of relative rock strength and air permeability indicate that lithofacies B is approximately three times less competent than both lithofacies A and C, and it is characterized by a permeability one order of magnitude higher than them. Although deformation bands occur within lithofacies B, locally enhancing cohesion through grain interlocking and comminution, these structures do not significantly increase the overall stiffness of the rock

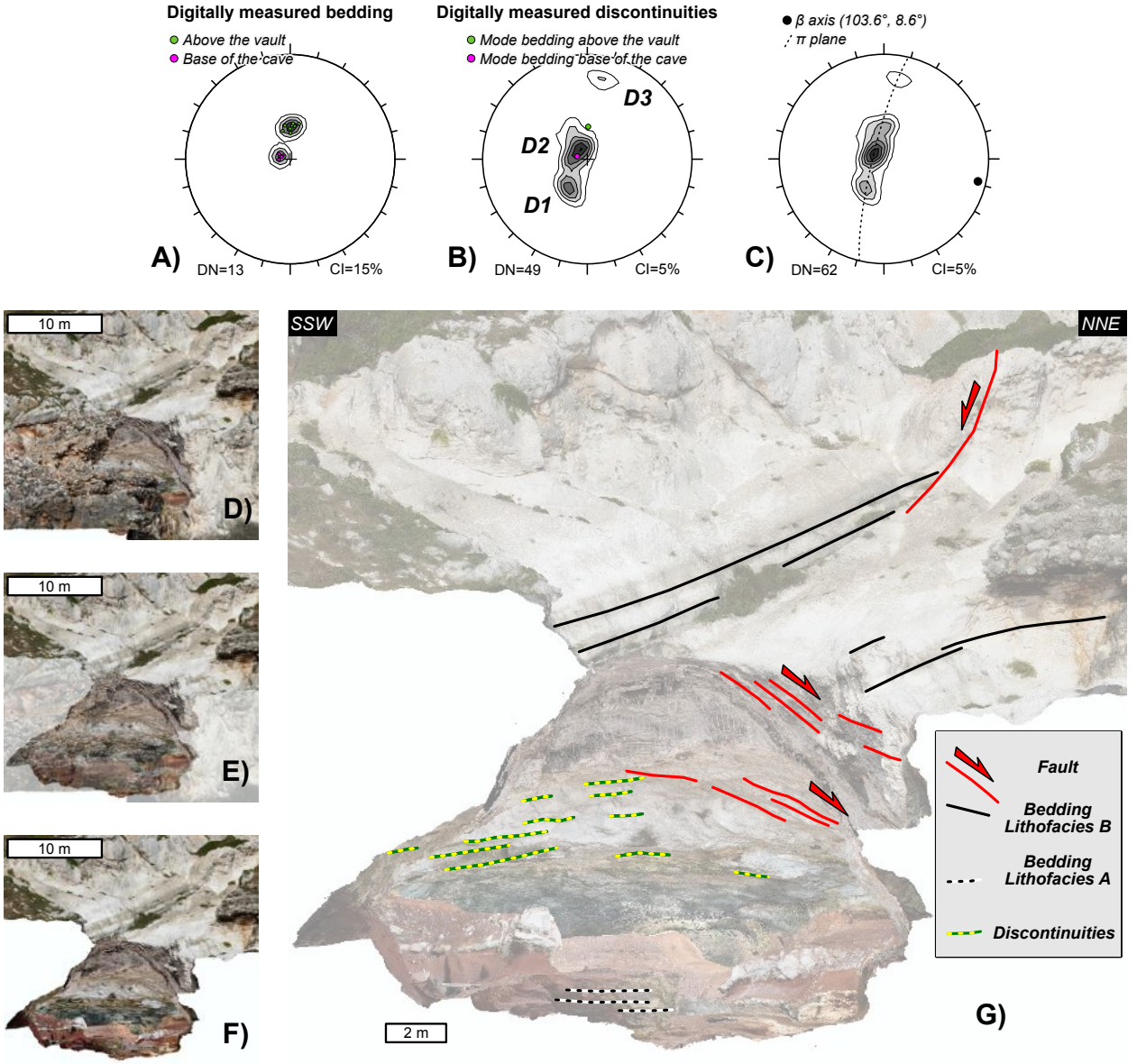

Figure 10. Structural data from integrated field and digital surveys of Grotta Romanelli. (A) Digitally measured bedding attitudes at the cave floor and immediately above the roof. DN—Data number; CI—Contouring interval. (B) Digitally measured planar discontinuities exposed on the cave vault and walls, showing three distinct sets. (C) Computed β axis (trend N103°E, plunge 8°) derived from bedding and discontinuity measurements in A and B. (D–F) Orthorectified images of the cave and its entrance, produced by using the β axis as the viewing direction and digitally removing the Quaternary breccia partly occluding the entrance, revealing the geometry of the structural discontinuities controlling the cave vault. (G) Interpretation of the orthorectified image.

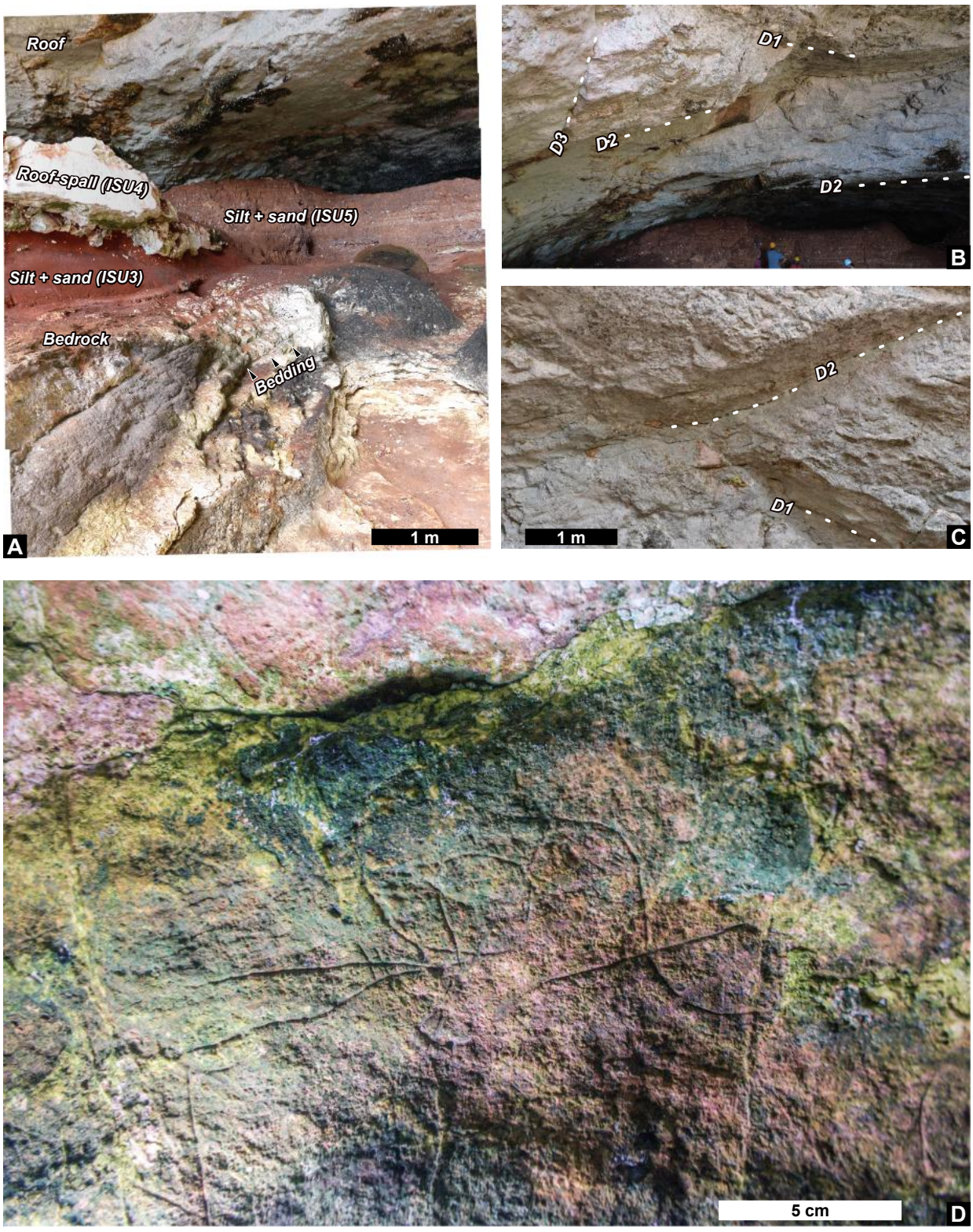

Figure 11. (A) Photomosaic showing the bedrock (base and vault) and infill of Grotta Romanelli, with the roof spall layer embedded within the Quaternary clastic infilling of the cave (labels for Quaternary deposits are from Pieruccini et al., 2022). (B) Discontinuities exposed along the cave vault, corresponding to the clusters delineated in Figure 10B. (C) Close-up view of discontinuities at the vault of the cave. (D) Example of parietal art developed along one of these discontinuity surfaces.

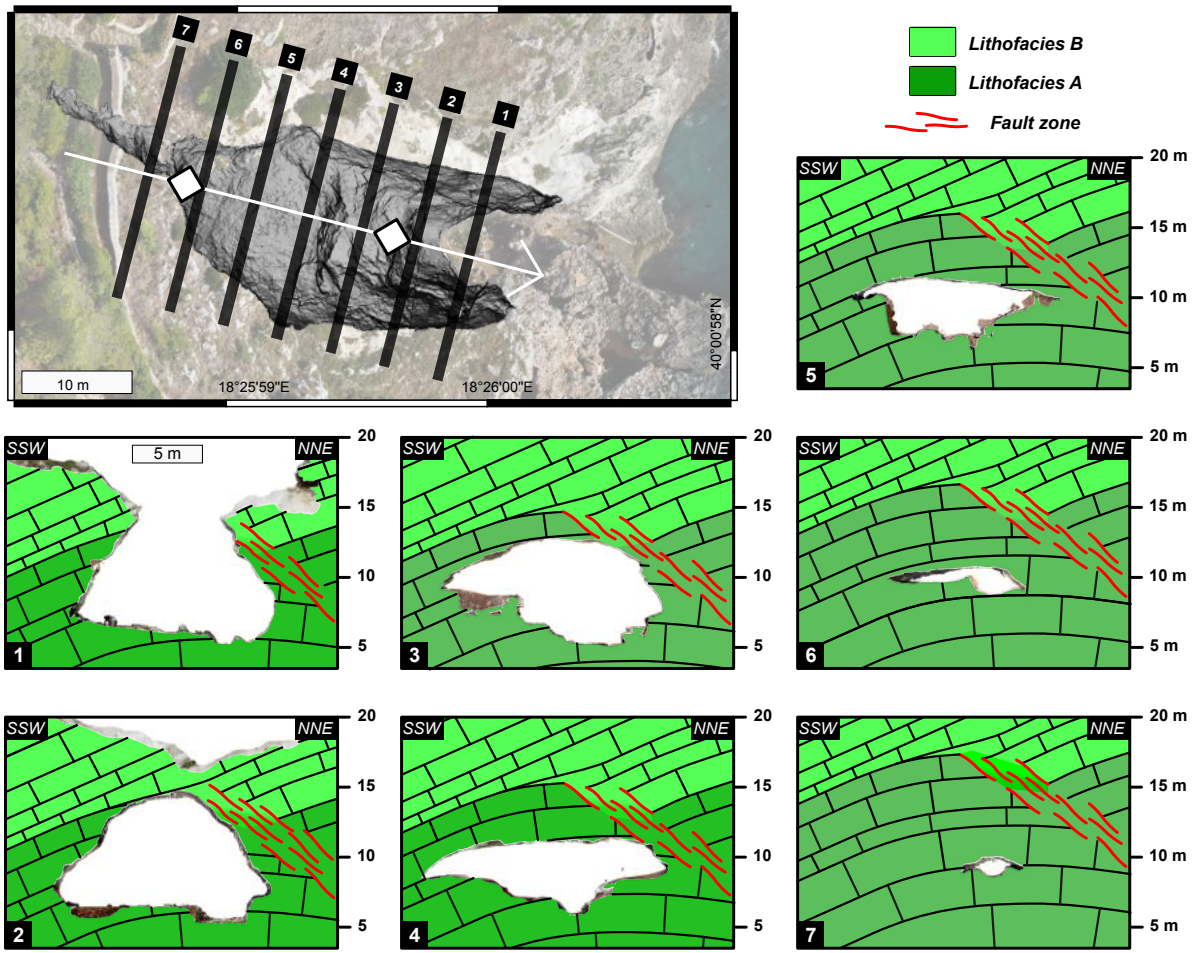

Figure 12. Map of the cave area, showing the hill-shaded digital elevation model of the cave in multidirectional illumination. The seven vertical geological cross sections are indicated, with their traces oriented parallel to the trend of the β axis derived in Figure 6.

mass. On the contrary, their cumulative effect promotes marked differential weathering and progressive weakening of the host rock. As a result, lithofacies B behaves as a mechanically soft layer, prone to strain concentration and time-dependent degradation. These properties exert a primary control on both the local stress distribution and the structural evolution of the cave.

Preliminary results from the FEM analysis, although based on approximate input parameters, provide a validation of the structural control exerted by the Cretaceous tectono-sedimentary framework. The model indicates that the cave vault is generally not subjected to instability conditions. However, strain concentrations are predicted at the entrance of the cave, in the area where the vault progressively thins and the narrow bridge connecting the two flanks is almost entirely composed of lithofacies B. These localized zones of elevated stress correspond to the mechanically weakest portion of the roof, as quantified through the integration of Schmidt hammer–derived properties and air permeability values, where instability could preferentially develop under natural or anthropogenic perturbations.

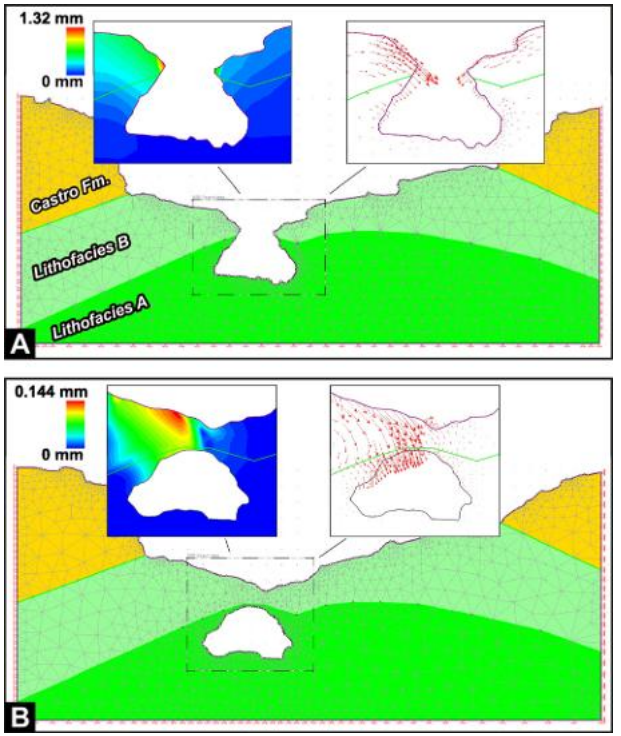

Figure 13. Finite element method (FEM) models generated with PHASE² software. The large panels show the FEM mesh, while the smaller windows illustrate the total estimated displacement, highlighting zones of displacement localization (contours) and displacement vectors (red arrows). (A) Model corresponding to section 1 in Figure 12. (B) Model corresponding to section 2 in Figure 12. Rock mass mechanical properties adopted for each lithological unit are reported in Supplemental Text S2 (see text footnote 1).

5.3 Structural Control on Cave Morphology and Stability

Preliminary FEM results indicate that the cave vault may be relatively stable, but this assessment assumes a mechanically homogeneous rock mass. In contrast, Grotta Romanelli formed along the axis of an anticline (likely an extensional fault–related anticline), where pronounced structural heterogeneity exerts a first-order control on cave development and stability. In this regard, the mechanical contrast between lithofacies A and B is not merely a sedimentological feature but represents a mechanical template inherited from the Cretaceous tectono-sedimentary framework.

The longitudinal sections of the cave (Fig. 12) show a geometric correspondence between the cave profile, the bedding planes exposed along the southern wall and the vault, and the fault zone exposed along the northern wall. Bedding planes and fault surfaces, together with the alignment of the cave along the fold axis, played a key role in shaping the cave morphology by promoting successive slab-detachment events from the vault and, locally, from the walls (Palmer, 2007; De Waele and Gutiérrez, 2022). The largest of these events correspond to the two roof-spall deposits (ISU 2 and ISU 4 in Fig. 11A), which influenced the clastic sedimentation within the cave and are reflected in the stepped geometry of the vault, where each break marks a former collapse surface. In addition to this structural control, mechanical breakdown related to freeze-thaw cycles and biological weathering processes likely contributed to the progressive disintegration of the vault (and walls).

On the other hand, both deformation bands in lithofacies B and joints in lithofacies A introduce an additional level of structural control, displaying a dual hydraulic behavior. Deformation bands in carbonates commonly act as barriers to cross-fault fluid flow due to porosity collapse, and localized microstylolites and grain interpenetration (Tondi et al., 2012, 2016), or deviate flow lines according to their spatial arrangement (Antonellini et al., 2014). In contrast, joints in carbonates enhance fluid circulation in a direction parallel to the fracture planes (Aydin, 2000), depending upon their degree of connectivity (Agosta et al., 2010) and diagenetic evolution (Laubach et al., 2010). Furthermore, we interpret the WNW-ESE–striking fault zone bounding the northern side of the cave, irrespective of whether it cuts lithofacies A or B, as forming localized conduits for fault-parallel fluid flow (Caine et al., 1996). This fluid conduit promoted dissolution and preferential widening along the longitudinal axis of the cave, thereby reinforcing its structural alignment. Our air-permeability measurements (Fig. 9) support this interpretation, showing that the porous lithofacies B within the WNW-ESE–striking damage zone likely provided a preferential pathway for carbonate dissolution. This explains the longitudinal alignment of the cave along the fold axis, as the structural backbone provided both the chemical (permeability) and mechanical (weakness) path of least resistance for karstification.

The structural control at Grotta Romanelli follows a pattern observed in major karst systems where fold hinges and fracture corridors are preferential sites for dissolution (Ennes-Silva et al., 2016; Bagni et al., 2020; Abolins et al., 2025). However, the link between speleogenesis and structure is particularly subtle at Grotta Romanelli, as the Cretaceous tectonic inheritance consists of embryonic, synsedimentary features and soft-sediment deformation structures not easily detectable in the field. It is only through the "magnifying glass" of petrophysical characterization and structural analysis, integrated by high-resolution digital models bridging the gap between "inside" and "outside" surveys, that even a subtle, inherited tectonic template can provide the primary backbone for speleogenesis, and long-term morphological evolution and stability of a cavity.

5.4 Methodological Implications

The study of Grotta Romanelli demonstrates the effectiveness of combining detailed structural fieldwork with virtual outcrop analysis (e.g., McCaffrey et al.,

2005; Jones et al., 2009; Bistacchi et al., 2015; Burnham and Hodgetts, 2019; Bond and Cawood, 2021; Buckley et al., 2022; Del Rio et al., 2025). A thorough and multiscale characterization of complex geological sites can be made by integrating traditional field-based geological survey techniques with VOMs, guaranteeing that interpretation is both field-anchored and quantitatively constrained. VOMs now represent a central component of structural geology workflows, allowing quantitative and metric analyses that were previously unattainable through conventional methods. The extraction of orthorectified images along geologically meaningful planes or viewing directions provides an immediate and effective tool to quantify structural geometries and spatial relationships (Tavani et al., 2016; Cawood et al., 2022). However, the scientific value of these digital tools is critically dependent on an expert-based approach, and sound structural reasoning is needed to capture the tectonic significance of the observed features.

This approach situates itself within the ongoing debate on the balance between digital and traditional methods in geosciences (e.g., Pavlis et al., 2010; Pavlis and Mason, 2017; Walker et al., 2019; Whitmeyer et al., 2019; Tavani et al., 2022), emphasizing that progress lies not in replacing fieldwork but in strengthening its analytical depth through quantitative tools. In this perspective, the workflow adopted for Grotta Romanelli may serve as a methodological reference for future studies conducted in similarly complex and constrained geological settings.

5.5 Geological and Heritage Implications

Beyond its geological interest, the 3-D reconstruction of Grotta Romanelli has direct implications for the conservation and management of karst heritage sites. Caves of this type, developed in carbonates, are widespread across the Mediterranean region and frequently host valuable paleontological, archaeological, or geomorphological archives. A robust geological and structural framework is essential to assess their stability, understand their long-term evolution, and plan future scientific investigations or public access. In this context, the FEM modeling is not merely a tectonic exercise but a necessary tool for heritage management. By pinpointing where the stress field interacts with preexisting Cretaceous discontinuities, we can predict which areas of the Paleolithic parietal art or stratigraphic deposits are most at risk from future roof-spalling events. This approach provides a reproducible workflow that can be applied to similar sites, enhancing both their protection and their scientific usability.

6. CONCLUSIONS

This study provides the first integrated structural and stratigraphic characterization of the bedrock of Grotta Romanelli, southern Italy. Supported by a high-resolution 3-D model of the cave and its host rock, the results of these multidisciplinary analyses defined the structural setting of the site and clarified the relations among synkinematic faulting, fracturing, lithology, and cave morphology. In particular, the results show that the cave developed within a Cretaceous synsedimentary structural framework, which exerted a primary control on its speleogenesis.

The integration of field observations and VOM offers a robust basis for evaluating the stability and long-term evolution of the cave, improving the interpretation of its paleontological and archaeological record. More broadly, the approach adopted here provides a reproducible workflow applicable to similar karst heritage sites, where a sound geological framework is essential for conservation, scientific investigation, and potential enhancement for cultural or educational purposes.

ACKNOWLEDGMENTS

We thank Associate Editor Michelangelo Martini, Steve Whitmeyer, and an anonymous reviewer for their constructive comments that helped to improve the manuscript. We acknowledge Agisoft for the academic license for Metashape 2.2.2. This work was funded by Sapienza Università di Roma with Finanziamento Ricerche di Ateneo Grandi Scavi 2023 (grant SA1231888AE771CD) and Grandi Scavi 2024 (grant SA12419011BD11EF). R. Sardella thanks Petroleum Experts (Petex) for providing the 3DMove software suite used for the kinematic restorations. A downsampled version of the 3-D virtual outcrop model is available at the v3Geo repository (https://v3geo.com/model/980/edit/info). The StraboSpot file containing field measurements, photos, and sketches is available at https://strabospot.org/doi/detail/14147c73-f0db-4b9a-a254-8c2747393cd6.

REFERENCES CITED

Abolins, M., Firkaly-Paciera, J., King, B., Ocasio-Valentin, C., Slighter, J., Sullivan, T., and Whited, J., 2025, The relationship between lineaments and cave passages in unfaulted gently folded strata, Snail Shell Cave, central Tennessee, USA: International Journal of Speleology, v. 54, no. 2, https://doi.org/10.5038/1827-806X.ijs2544.

Agosta, F., Alessandroni, M., Antonellini, M., Tondi, E., and Giorgioni, M., 2010, From fractures to flow: A field-based quantitative analysis of an outcropping carbonate reservoir: Tectonophysics, v. 490, no. 3–4, p. 197–213, https://doi.org/10.1016/j.tecto.2010.05.005.

Agosta, F., Manniello, C., Cavalcante, F., Belviso, C., and Prosser, G., 2021, Late Cretaceous transtensional faulting of the Apulian Platform, Italy: Marine and Petroleum Geology, v. 127, https://doi.org/10.1016/j.marpetgeo.2020.104889.

Agosta, F., Petrullo, A.V., La Bruna, V., and Prosser, G., 2023, Cenozoic fault growth mechanisms in the outer Apulian Platform: Geosciences, v. 13, no. 4, 121, https://doi.org/10.3390/geosciences13040121.

Antonellini, M., Tondi, E., Agosta, F., Aydin, A., and Cello, G., 2008, Failure modes in deep-water carbonates and their impact for fault development: Majella Mountain, Central Apennines, Italy: Marine and Petroleum Geology, v. 25, no. 10, p. 1074–1096, https://doi.org/10.1016/j.marpetgeo.2007.10.008.

Antonellini, M., Cilona, A., Tondi, E., Zambrano, M., and Agosta, F., 2014, Fluid flow numerical experiments of faulted porous carbonates, northwest Sicily (Italy): Marine and Petroleum Geology, v. 55, p. 186–201, https://doi.org/10.1016/j.marpetgeo.2013.12.003.

Antonellini, M., Nannoni, A., Vigna, B., and De Waele, J., 2019, Structural control on karst water circulation and speleogenesis in a lithological contact zone: The Bossea cave system (western Alps, Italy): Geomorphology, v. 345, https://doi.org/10.1016/j.geomorph.2019.07.019.

Antonioli, F., Ferranti, L., Stocchi, P., Deiana, G., Lo Presti, V., Furlani, S., Marino, C., Orru, P., Scicchitano, G., Trainito, E., Anzidei, M., Bonamini, M., Sansò, M., Sansò, P., and Mastronuzzi, G., 2018, Morphometry and elevation of the last interglacial tidal notches in tectonically stable coasts of the Mediterranean Sea: Earth-Science Reviews, v. 185, p. 600–623, https://doi.org/10.1016/j.earscirev.2018.06.017.

Argnani, A., Favalli, P., Frugoni, F., Gasperini, M., Ligi, M., Marani, M., Mattietti, G., and Mele, G., 1993, Foreland deformational pattern in the southern Adriatic Sea: Annales Geophysicae, v. 36, no. 2, p. 229–247, https://doi.org/10.4401/ag-4279.

Aydin, A., 2000, Fractures, faults, and hydrocarbon entrapment, migration and flow: Marine and Petroleum Geology, v. 17, no. 7, p. 797–814, https://doi.org/10.1016/S0264-8172(00)00020-9.

Bagni, F.L., Bezerra, F.H., Balsamo, F., Maia, R.P., and Dall'Aglio, M., 2020, Karst dissolution along fracture corridors in an anticline hinge, Jandaíra Formation, Brazil: Implications for reservoir quality: Marine and Petroleum Geology, v. 115, https://doi.org/10.1016/j.marpetgeo.2020.104249.

Basilone, L., and Sulli, A., 2018, Basin analysis in the southern Tethyan margin: Facies sequences, stratal pattern and subsidence history highlight extension-to-inversion processes in the Cretaceous Panormide carbonate platform (NW Sicily): Sedimentary Geology, v. 363, p. 235–251, https://doi.org/10.1016/j.sedgeo.2017.11.013.

Benjamin, J., Rovere, A., Fontana, A., Furlani, S., Vacchi, M., Inglis, R.H., Galili, E., Antonioli, F., Sivan, D., Miko, S., Mourtzas, N., Felja, I., Meredith-Williams, M., Goodman-Tchernov, B., Kolaiti, E., Anzidei, M., and Gehrels, R., 2017, Late Quaternary sea-level changes and early human societies in the central and eastern Mediterranean Basin: An interdisciplinary review: Quaternary International, v. 449, p. 29–57, https://doi.org/10.1016/j.quaint.2017.06.025.

Bernoulli, D., 2001, Mesozoic–Tertiary carbonate platforms, slopes and basins of the external Apennines and Sicily, *in* Vai, G.B., and Martini, I.P., eds., Anatomy of an Orogen: The Apennines and Adjacent Mediterranean Basins: Dordrecht, Netherlands, Kluwer Academic Publishers, p. 307–325, https://doi.org/10.1007/978-94-015-9829-3_18.

Bertok, C., Capizzi, R., Martire, L., and Dela Pierre, F., 2012, The Cretaceous–Eocene succession of the Rocca Busambra (western Sicily, Italy): A patchy record on a dissected palaeostructural high: Italian Journal of Geosciences, v. 131, no. 1, p. 32–46, https://doi.org/10.3301/IJG.2011.21.

Billi, A., and Salvini, F., 2003, Development of systematic joints in response to flexure-related fibre stress in flexed foreland plates: The Apulian forebulge case history, Italy: Journal of Geodynamics, v. 36, p. 523–536, https://doi.org/10.1016/S0264-3707(03)00086-3.

Bistacchi, A., et al., 2015, Photogrammetric digital outcrop reconstruction, visualization with textured surfaces, and three-dimensional structural analysis and modeling: Innovative methodologies applied to fault-related dolomitization (Vajont limestone, southern Alps, Italy): Geosphere, v. 11, p. 2031–2048, https://doi.org/10.1130/GES01005.1.

Blanc, G.A., 1920, Grotta Romanelli I. Stratigrafia dei depositi e natura e origine di essi: Archivo per l'Antropologia e la Etnologia, v. 50, p. 1–39.

Boersma, Q., Prabhakaran, R., Bezerra, F.H., and Bertotti, G., 2019, Linking natural fractures to karst cave development: A case study combining drone imagery, a natural cave network and numerical modelling: Petroleum Geoscience, v. 25, no. 4, p. 454–469, https://doi.org/10.1144/petgeo2018-151.

Bond, C., and Cawood, A., 2021, A role for virtual outcrop models in blended learning—Improved 3D thinking and positive perceptions of learning: Geoscience Communication, v. 4, no. 2, p. 233–244, https://doi.org/10.5194/gc-4-233-2021.

Bosellini, A., Bosellini, F.R., Colalongo, M.L., Parente, M., Russo, A., and Vescogni, A., 1999, Stratigraphic architecture of the Salento coast from Capo d'Otranto to S. Maria di Leuca (Apulia, southern Italy): Rivista Italiana di Paleontologia e Stratigrafia, v. 105, p. 397–416, https://doi.org/10.13130/2039-4942/5382.

Bosellini, F.R., and Russo, A., 1992, Stratigraphy and facies of an Oligocene fringing reef (Castro Limestone, Salento Peninsula, southern Italy): Facies, v. 26, p. 145–165, https://doi.org/10.1007/BF02539798.

Buckley, S., et al., 2022, V3geo: A cloud-based repository for virtual 3D models in geoscience: Geoscience Communication, v. 5, no. 1, p. 67–82, https://doi.org/10.5194/gc-5-67-2022.

Burnham, B., and Hodgetts, D., 2019, Quantifying spatial and architectural relationships from fluvial outcrops: Geosphere, v. 15, p. 236–253, https://doi.org/10.1130/GES01574.1.

Caine, J.S., Evans, J.P., and Forster, C.B., 1996, Fault zone architecture and permeability structure: Geology, v. 24, p. 1025–1028, https://doi.org/10.1130/0091-7613(1996)024%3C1025:FZAAPS%3E2.3.CO;2.

Carandini, L., and Biddittu, I., 1967, Attività scientifica dell'Istituto Italiano di Paleontologia Umana dalla sua fondazione, VI - Puglia: Quaternaria, v. 9, p. 385–408. Rome, Italy. Istituto Italiano di Paleontologia Umana.

Cardini, L., 1963, Presentazione delle industrie musteriane su calcare dei livelli a terre rossa di Grotta Romanelli, *in* Atti dell'VIII riunione dell'istituto di Preistoria e Protostoria, Trieste, Italy, 43 p.

Cassoli, F., and Tagliacozzo, A., 1997, Butchering and cooking of birds in the Palaeolithic site of Grotta Romanelli (Italy): International Journal of Osteoarchaeology, v. 7, p. 303–320, https://doi.org/10.1002/(SICI)1099-1212(199707/08)7:4<303::AID-OA380>3.0.CO;2-R.

Cawood, A.J., Corradetti, A., Granado, P., and Tavani, S., 2022, Detailed structural analysis of digital outcrops: A learning example from the Kermanshah-Qulqula radiolarite basin, Zagros belt, Iran: Journal of Structural Geology, v. 154, https://doi.org/10.1016/j.jsg.2021.104489.

Cipriani, A., 2016, Geology of the Mt. Cosce sector (Narni Ridge, Central Apennines, Italy): Journal of Maps, v. 12, p. 328–340, https://doi.org/10.1080/17445647.2016.1211896.

Coleman, A.J., Duffy, O.B., and Jackson, C.A.L., 2019, Growth folds above propagating normal faults: Earth-Science Reviews, v. 196, https://doi.org/10.1016/j.earscirev.2019.102885.

Comina, C., Motta, M., Muzzolon, W., Vagnon, F., and Vergnano, A., 2024, Challenging underground geophysical, geological and topographical surveys in the Borna Maggiore di Pugnetto karst collapse cave to delineate its genesis and actual structure: Earth Surface Processes and Landforms, v. 49, no. 15, p. 5390–5405, https://doi.org/10.1002/esp.6023.

Del Rio, M., Corradetti, A., Černok, A., Narduzzi, F., Venier, M., and Ziberna, L., 2025, Virtual outcrop modelling and petrography of a heterogeneous gabbroic outcrop in the Ivrea-Verbano zone, Italy: Geological Magazine, v. 162, p. e35, https://doi.org/10.1017/S001675682510023X.

De Waele, J., and Gutiérrez, F., 2022, Karst Hydrogeology, Geomorphology and Caves: New York, John Wiley & Sons, https://doi.org/10.1002/9781119605379.

Ennes-Silva, R.A., Bezerra, F.H.R., Nogueira, F.C.C., Balsamo, F., Klimchouk, A., Cazarin, C.L., and Auler, A.S., 2016, Superposed folding and associated fracturing influence hypogene karst development in Neoproterozoic carbonates, São Francisco craton, Brazil: Tectonophysics, v. 666, p. 244–259, https://doi.org/10.1016/j.tecto.2015.11.006.

Festa, V., 2003, Cretaceous structural features of the Murge area (Apulian foreland, southern Italy): Eclogae Geologicae Helvetiae, v. 96, p. 11–22, https://doi.org/10.5169/seals-169003.

Ford, D.C., and Williams, P.W., 2007, Karst Hydrogeology and Geomorphology: Chichester, UK, Wiley-Blackwell, 562 p., https://doi.org/10.1002/9781118684986.

Fornaca-Rinaldi, G., 1968, Il metodo $^{230}Th/^{238}U$ per la datazione di stalattiti e stalagmiti: Bollettino di Geofisica Teorica ed Applicata, v. 10, p. 3–14.

Goldscheider, N., and Neukum, C., 2010, Fold and fault control on the drainage pattern of a double-karst-aquifer system, Winterstaude, Austrian Alps: Acta Carsologica, v. 39, no. 2, https://doi.org/10.3986/ac.v39i2.91.

Goodman, R.E., 1989, Introduction to Rock Mechanics (2nd edition): New York, John Wiley and Sons, 576 p.

Graziano, R., 2000, The Aptian–Albian of the Apulia carbonate platform (Gargano Promontory, southern Italy): Evidence of palaeoceanographic and tectonic controls on the stratigraphic architecture of the platform margin: Cretaceous Research, v. 21, no. 1, p. 107–126, https://doi.org/10.1006/cres.2000.0201.

Jones, R.R., et al., 2009, Integration of regional to outcrop digital data: 3D visualisation of multi-scale geological models: Computers & Geosciences, v. 35, no. 1, p. 4–18, https://doi.org/10.1016/j.cageo.2007.09.007.

Katz, O., Reches, Z., and Roegiers, J.C., 2000, Evaluation of mechanical rock properties using a Schmidt Hammer: International Journal of Rock Mechanics and Mining Sciences, v. 37, no. 4, p. 723–728, https://doi.org/10.1016/S1365-1609(00)00004-6.

Lash, G.G., and Engelder, T., 2007, Jointing within the outer arc of a forebulge at the onset of the Alleghanian orogeny: Journal of Structural Geology, v. 29, no. 5, p. 774–786, https://doi.org/10.1016/j.jsg.2006.12.002.

Laubach, S.E., Eichhubl, P., Hilgers, C., and Lander, R.H., 2010, Structural diagenesis: Journal of Structural Geology, v. 32, no. 12, p. 1866–1872, https://doi.org/10.1016/j.jsg.2010.10.001.

Mastronuzzi, G., Quinif, Y., Sansò, P., and Selleri, G., 2007, Middle–late Pleistocene polycyclic evolution of a stable coastal area (southern Apulia, Italy): Geomorphology, v. 86, p. 393–408, https://doi.org/10.1016/j.geomorph.2006.09.014.

McCaffrey, K.J.W., et al., 2005, Unlocking the spatial dimension: Digital technologies and the future of geoscience fieldwork: Journal of the Geological Society, v. 162, no. 6, p. 927–938, https://doi.org/10.1144/0016-764905-017.

Palmer, A.N., 1989, Stratigraphic and structural control of cave development and groundwater flow in the Mammoth Cave region, *in* White, W.B., and White, E.L., eds., Karst Hydrology: Concepts from the Mammoth Cave Area: Boston, Massachusetts, USA, Springer, p. 293–316, https://doi.org/10.1007/978-1-4615-7317-3_11.

Palmer, A.N., 2007, Cave Geology: Dayton, Ohio, Cave Books, 454 p.

Parente, M., 1994, A revised stratigraphy of the Upper Cretaceous to Oligocene units of southeastern Salento (Apulia, southern Italy): Bollettino della Società Paleontologica Italiana, v. 33, no. 2, p. 1–16.

Pavlis, T.L., and Mason, K.A., 2017, The new world of 3D geologic mapping: GSA Today, v. 27, no. 9, p. 4–10, https://doi.org/10.1130/GSATG313A.1.

Pavlis, T.L., Langford, R., Hurtado, J., and Serpa, L., 2010, Computer-based data acquisition and visualization systems in field geology: Results from 12 years of experimentation and future potential: Geosphere, v. 6, p. 275–294, https://doi.org/10.1130/GES00503.S2.

Pennos, C., et al., 2019, From subsurface to surface: A multidisciplinary approach to decoding uplift histories in tectonically-active karst landscapes: Earth Surface Processes and Landforms, v. 44, no. 9, p. 1710–1721, https://doi.org/10.1002/esp.4605.

Pieruccini, P., Forti, L., Mecozzi, B., Iannucci, A., Yu, T.-L., Shen, C.-C., Bona, F., Lembo, G., Muttillo, B., Sardella, R., and Mazzini, I., 2022, Stratigraphic reassessment of Grotta Romanelli sheds light on middle–late Pleistocene palaeoenvironments and human settling in the Mediterranean: Scientific Reports, v. 12, https://doi.org/10.1038/s41598-022-16906-9.

Pomar, L., Mateu-Vicens, G., Morsilli, M., and Brandano, M., 2014, Carbonate ramp evolution during the late Oligocene (Chattian), Salento Peninsula, southern Italy: Palaeogeography, Palaeoclimatology, Palaeoecology, v. 404, p. 109–132, https://doi.org/10.1016/j.palaeo.2014.03.023.

Ricchetti, G., Ciaranfi, N., Luperto Sinni, E., Mongelli, F., and Pieri, P., 1988, Geodinamica ed evoluzione sedimentaria e tettonica dell'Avampaese apulo: Memorie della Societa Geologica Italiana, v. 41, p. 57–82.

Santaloia, F., Zuffianò, L.E., Palladino, G., Limoni, P.P., Liotta, D., Minissale, A., Brogi, A., and Polemio, M., 2016, Coastal thermal springs in a foreland setting: The Santa Cesarea Terme system (Italy): Geothermics, v. 64, p. 344–361, https://doi.org/10.1016/j.geothermics.2016.06.013.

Santantonio, M., Scrocca, D., and Lipparini, L., 2013, The Ombrina-Rospo Plateau (Apulian Platform): Evolution of a carbonate platform and its margins during the Jurassic and Cretaceous: Marine and Petroleum Geology, v. 42, p. 4–29, https://doi.org/10.1016/j.marpetgeo.2012.11.008.

Sardella, R., Iurino, D.A., Mecozzi, B., Sigari, D., Bona, F., Bellucci, L., Coltorti, M., Conti, J., Lembo, G., Muttillo, B., and Mazzini, I., 2019, Grotta Romanelli (Lecce, southern Italy) between past and future: New studies and perspectives for an archaeo-geosite symbol of the Palaeolithic in Europe: Geoheritage, v. 11, no. 4, p. 1413–1432, https://doi.org/10.1007/s12371-019-00376-z.

Schlüter, M., Steuber, T., and Parente, M., 2008, Chronostratigraphy of Campanian–Maastrichtian platform carbonates and rudist associations of Salento (Apulia, Italy): Cretaceous Research, v. 29, p. 100–114, https://doi.org/10.1016/j.cretres.2007.04.005.

Sigari, D., Bourdier, C., Conti, C., Conti, J., Forti, L., García-Diez, M., Lai, G., Mazzini, I., Pieruccini, P., and Sardella, R., 2024, The last cave lion of the late Upper Palaeolithic: The engraved feline of Grotta Romanelli (southern Italy): Quaternary Science Reviews, v. 334, https://doi.org/10.1016/j.quascirev.2024.108670.

Silva, O.L., Bezerra, F.H., Maia, R.P., and Cazarin, C.L., 2017, Karst landforms revealed at various scales using LiDAR and UAV in semi-arid Brazil: Consideration on karstification processes and methodological constraints: Geomorphology, v. 295, p. 611–630, https://doi.org/10.1016/j.geomorph.2017.07.025.

Stasi, P.E., and Regalia, E., 1904, Grotta Romanelli stazione con faune interglaciali calde e di steppa. Nota preventiva: Società Italiana di Antropologia, v. 1, p. 17–81.

Tavani, S., Corradetti, A., and Billi, A., 2016, High precision analysis of an embryonic extensional fault–related fold using 3D orthorectified virtual outcrops: The viewpoint importance in structural geology: Journal of Structural Geology, v. 86, p. 200–210, https://doi.org/10.1016/j.jsg.2016.03.009.

Tavani, S., Corradetti, A., Granado, P., Snidero, M., Seers, T.D., and Mazzoli, S., 2019, Smartphone: An alternative to ground control points for orienting virtual outcrop models and assessing their quality: Geosphere, v. 15, p. 2043–2052, https://doi.org/10.1130/GES02167.1.

Tavani, S., et al., 2022, Smartphone assisted fieldwork: Towards the digital transition of geoscience fieldwork using LiDAR-equipped iPhones: Earth-Science Reviews, v. 227, https://doi.org/10.1016/j.earscirev.2022.103969.

Tavani, S., et al., 2023, Post-rift Aptian–Cenomanian extension in Adria, insight from the km-scale Positano–Vico Equense syn-sedimentary fault: Journal of Structural Geology, v. 168, https://doi.org/10.1016/j.jsg.2023.104820.

Tema, E., Lanci, L., Mariani, G.S., Pieruccini, P., Mazzini, I., and Sardella, R., 2025, Late Pleistocene–Holocene paleosecular variation dating of cave sediments: Insights from Grotta Romanelli (Apulia, Italy): Geochemistry, Geophysics, Geosystems, v. 26, no. 7, https://doi.org/10.1029/2024GC012148.

Tondi, E., Cilona, A., Agosta, F., Aydin, A., Rustichelli, A., Renda, P., and Giunta, G., 2012, Growth processes, dimensional parameters and scaling relationships of two conjugate sets of compactive shear bands in porous carbonate grainstones, Favignana Island, Italy: Journal of Structural Geology, v. 37, p. 53–64, https://doi.org/10.1016/j.jsg.2012.02.003.

Tondi, E., Rustichelli, A., Cilona, A., Balsamo, F., Storti, F., Napoli, G., Agosta, F., and Giorgioni, M., 2016, Hydraulic properties of fault zones in porous carbonates, examples from central and southern Italy: Italian Journal of Geosciences, v. 135, no. 1, p. 68–79, https://doi.org/10.3301/IJG.2015.08.

Verhoeven, G., 2011, Taking computer vision aloft—Archaeological three-dimensional reconstructions from aerial photographs with photoscan: Archaeological Prospection, v. 18, no. 1, p. 67–73, https://doi.org/10.1002/arp.399.

Walker, J.D., et al., 2019, StraboSpot data system for structural geology: Geosphere, v. 15, p. 533–547, https://doi.org/10.1130/GES02039.1.

White, W.B., 1988, Geomorphology and Hydrology of Karst Terrains: Oxford, UK, Oxford University Press, 480 p.

Whitmeyer, S.J., Pyle, E.J., Pavlis, T.L., Swanger, W., and Roberts, L., 2019, Modern approaches to field data collection and mapping: Digital methods, crowdsourcing, and the future of statistical analyses: Journal of Structural Geology, v. 125, p. 29–40, https://doi.org/10.1016/j.jsg.2018.06.023.

Xiao, P., Yang, X., Li, B., Zhou, X., Sun, Y., Ding, X., and Xu, N., 2025, Roof arch collapse of underground cavern in fractured rock mass: In situ monitoring and numerical modeling: Journal of Rock Mechanics and Geotechnical Engineering, v. 17, no. 5, p. 2778–2792, https://doi.org/10.1016/j.jrmge.2024.05.018.

Zhao, M., and Jacobi, R.D., 1997, Formation of regional cross-fold joints in the northern Appalachian Plateau: Journal of Structural Geology, v. 19, no. 6, p. 817–834, https://doi.org/10.1016/S0191-8141(97)00009-6.